



RESEARCH ARTICLE

10.1029/2020JD033126

Key Points:

- Our new LOFAR imaging procedure can locate over 200 sources per millisecond of flash with meter-scale accuracy
- The primary initial leader breaks up into many (>10) negative leaders of which only one or two continue after 30 ms
- Some negative leaders propagate from the positive charge layer back to get close to the initiation point

Correspondence to:

O. Scholten,
O.Scholten@rug.nl

Citation:

Scholten, O., Hare, B. M., Dwyer, J., Sterpka, C., Kolmašová, I., Santolík, O., et al. (2021). The initial stage of cloud lightning imaged in high-resolution. *Journal of Geophysical Research: Atmospheres*, 126, e2020JD033126. <https://doi.org/10.1029/2020JD033126>

Received 19 MAY 2020

Accepted 12 JAN 2021

Author Contributions:

Conceptualization: B. M. Hare, J. Dwyer
Data curation: B. M. Hare, I. Kolmašová, O. Santolík, A. Corstanje, J. R. Hörandel, K. Mulrey, A. Nelles, T. N. G. Trinh
Formal analysis: J. Dwyer
Methodology: B. M. Hare, J. Dwyer, C. Sterpka
Software: B. M. Hare, A. Pel
Validation: B. M. Hare, J. Dwyer, C. Sterpka
Writing – review & editing: B. M. Hare, J. Dwyer

© 2021. The Authors.

This is an open access article under the terms of the [Creative Commons Attribution-NonCommercial-NoDerivs License](#), which permits use and distribution in any medium, provided the original work is properly cited, the use is non-commercial and no modifications or adaptations are made.

The Initial Stage of Cloud Lightning Imaged in High-Resolution

O. Scholten^{1,2,3} , B. M. Hare¹ , J. Dwyer⁴, C. Sterpka⁴, I. Kolmašová^{5,6} , O. Santolík^{5,6}, R. Lán⁵, L. Uhlir⁵, S. Buitink^{7,8}, A. Corstanje^{7,8}, H. Falcke^{7,9,10,11}, T. Huege^{8,12}, J. R. Hörandel^{7,8,9}, G. K. Krampah⁸, P. Mitra⁸, K. Mulrey⁸, A. Nelles^{13,14}, H. Pandya⁸ , A. Pel², J. P. Rachen⁸, T. N. G. Trinh¹⁵ , S. ter Veen¹⁰, S. Thoudam¹⁶, and T. Winchen¹¹

¹University Groningen, Kapteyn Astronomical Institute, Groningen, The Netherlands, ²KVI-Center for Advanced Radiation Technology, University Groningen, Groningen, The Netherlands, ³Interuniversity Institute for High-Energy, Vrije Universiteit Brussel, Brussels, Belgium, ⁴Department of Physics and Space Science Center (EOS), University of New Hampshire, Durham, NH, USA, ⁵Department of Space Physics, Institute of Atmospheric Physics of the Czech Academy of Sciences, Prague, Czechia, ⁶Faculty of Mathematics and Physics, Charles University, Prague, Czechia, ⁷Department of Astrophysics/IMAPP, Radboud University Nijmegen, Nijmegen, The Netherlands, ⁸Astrophysical Institute, Vrije Universiteit Brussel, Brussels, Belgium, ⁹NIKHEF, Science Park Amsterdam, Amsterdam, The Netherlands, ¹⁰Netherlands Institute of Radio Astronomy (ASTRON), Dwingeloo, The Netherlands, ¹¹Max-Planck-Institut für Radioastronomie, Bonn, Germany, ¹²Institut für Kernphysik, Karlsruhe Institute of Technology (KIT), Karlsruhe, Germany, ¹³Erlangen Center for Astroparticle Physics, Friedrich-Alexander-Universität Erlangen-Nürnberg, Erlangen, Germany, ¹⁴DESY, Zeuthen, Germany, ¹⁵Department of Physics, School of Education, Can Tho University Campus II, Can Tho City, Vietnam, ¹⁶Department of Physics, Khalifa University, Abu Dhabi, United Arab Emirates

Abstract With LOFAR we have been able to image the development of lightning flashes with meter-scale accuracy and unprecedented detail. We discuss the primary steps behind our most recent lightning imaging method. To demonstrate the capabilities of our technique we show and interpret images of the first few milliseconds of two intracloud flashes. In all our flashes, the negative leaders propagate in the charge layer below the main negative charge. Among several interesting features we show that in about 2 ms after initiation the primary initial leader triggers the formation of a multitude (>10) negative leaders in a rather confined area of the atmosphere. From these only one or two continue to propagate after about 30 ms to extend over kilometers horizontally while another may propagate back to the initiation point. We also show that normal negative leaders can transition into an initial leader like state, potentially in the presence of strong electric fields. In addition, we show some initial breakdown pulses that occurred during the primary initial leader, and even during two “secondary” initial leaders that developed out of stepped leaders.

1. Introduction

One of the key open questions in lightning science concerns the understanding of the processes that are fundamental to the initiation and early development of a lightning flash. In particular, it is not known what processes lead to the creation of the primary initial leader (PIL) channel and how that channel propagates. In recent years, the use of lightning mapping arrays (Edens et al., 2012; Rison et al., 1999) and very high frequency (VHF) radio interferometers (Rhodes et al., 1994; Stock et al., 2014; Yoshida et al., 2010) augmented with fast antennas and optical measurements (Hill et al., 2011; Montanya et al., 2015; Qi et al., 2016; Tran & Rakov, 2016) have led to the general picture that lightning initiation begins with an ionization event (Stolzenburg et al., 2020), which could be in the form of a powerful narrow bipolar event (Rison et al., 2016) or much weaker VHF source as seen in, e.g., Lyu et al. (2019) and Marshall et al. (2019). This is followed by an initial leader, as imaged very nicely in Lyu et al. (2016) in VHF. The initial leader propagation usually involves a series of large preliminary breakdown pulses (see, e.g., Kolmašová et al., 2014, 2018), after which normal negative stepped leader propagation is observed. The transition from the initial leader to a negative stepped leader has been observed in Stolzenburg et al. (2020) with high-speed video and in electric field change data. The relation between emitted VHF power, the signal of a broadband antenna and interferometry images for the initial leader has been investigated also in Krehbiel (2017) for New Mexico lightning flashes. Why negative leaders initially propagate in a different mode than the normal leader stepping seen

later in the flash is not understood. Furthermore, the positive leader is often not observed during the initiation process and only appears in radio data much later on after the negative leader is well developed.

With the present work we add very accurate images, obtained using LOFAR, showing the dynamics of Dutch thunderstorms. LOFAR (van Haarlem et al., 2013) is a software-phased array consisting of several thousand simple antennas that is primarily built for radio astronomy, see Section 2.1. Thunderstorms we have observed in the general area of the Dutch LOFAR stations (Dutch thunderstorms) differ from the thunderstorms seen in the United States (and most other places in the world) by the fact that all the flashes we have observed initiate at the bottom of the main negative charge layer, and then propagate down into the lower positive charge layer. For many flashes, including the two discussed more extensively in this work, we observe an extensive network of negative leaders which very rarely result in a ground stroke. It thus appears that the negative leaders become “trapped” in the potential well of the lower positive charge layer. To improve the insight in the dynamics of the lightning discharge immediately after initiation, we have improved our imaging technique over our earlier procedure (Hare et al., 2019) by greatly increasing the number of located VHF sources. In Section 2.2, we elucidate on the main improvements of our present imaging procedure.

Some detailed images of the initial stage of the lightning discharge are shown in Section 3, partially to demonstrate the capabilities of our present imager. We show images for two flashes, one from 2018 and one from 2019. The 2018 flash shows the typical initial development we have seen in all our imaged flashes, about 10 in number. The flash starts with a very small pulse in VHF, barely recognizable even with our sensitive LOFAR antennas. This develops into a PIL, as also imaged in Lyu et al. (2016). During its development we detect rapidly increasing VHF (30–80 MHz) activity reaching a maximum about 2 ms after initiation. It is known that low-frequency radiation is emitted in the initial stages of a flash (Kolmašová et al., 2018; Smith et al., 2018). For the 2019 flash, we also have low-frequency data recorded with a broadband magnetic loop antenna during the initial stage of the flash, showing significant broad-band emissions at particular stages of the PIL development. After descending down from the negative to the positive charge layer the PIL initiates a plethora of negative leaders almost simultaneously in an area of about 1 km². Of the original multitude of negative leaders, only one or two continue to propagate after about 30 ms to form the main part of the flash which may cover distances of 10 km or more. The 2019 flash is interesting since we see there is a PIL and even two secondary initial leaders (SIL). The initial leaders are clearly distinguishable from a negative leader through their propagation speed, a relatively low density of located sources and powerful VHF emission.

Some suggestions for a possible interpretation of our observations are presented in Section 4.

2. Methods

Our localization procedure for sources emitting pulses detected by LOFAR basically follows the structure outlined in Hare et al. (2019). Arrival time differences for pulses coming from the same source in different antennas are extracted from the data using the maxima in the cross-correlations. The present process incorporates important improvements that are mainly due to an improved procedure, inspired by that of the Kalman filter, to follow the pulse from the same source across many different antennas that may be many tens of kilometers apart. For completeness we outline here the procedure we followed (Scholten, 2020).

In this work, we use (interferometric) cross-correlations between small sections of the time traces to calculate the arrival time differences of pulses for each antenna with that of a reference antenna. From these arrival time differences in 100–400 antennas, we locate the position and time of the impulsive point source. We refer to the total of all these 4D source locations and times as the “image” of the flash. Some literature, where source locations are determined using the pulse arrival times as measured with a lightning mapping, refer to their result as a “map” of the flash. An alternatively view of our imaging procedure presented in this work is that “located sources” are in fact the most likely places of the maximum of an interferometric image for a small (0.1-μs long) section of the time trace centered around a pulse. Below we give a detailed outline of our procedure.

2.1. LOFAR

LOFAR (van Haarlem et al., 2013) is a radio telescope consisting of several thousand antennas. These antennas are spread over a large area with a dense core (a circular area with a diameter of 300 m, the Su-

perterp) near Exloo, The Netherlands. Remote stations spread over Europe, reaching baselines in excess of 1,000 km. The signals from these antennas can be added coherently to make this effectively operate as a gigantic radio dish, primarily used for radio astronomy. For our lightning observations, we confine ourselves to the LOFAR stations in the Netherlands, reaching baselines of the order of 100 km, see FLOFAR-NL. We use the low band antennas (LBAs) operating in the frequency range from 30 to 80 MHz. The LOFAR antennas are arranged in stations. Each station has 96 dual polarized antennas with an inverted V-shape. The signals are sampled at 200 MHz (5 ns sampling time). For our observations, we use about 12 antennas (6 for each polarization) per station. For the lightning observations, the circular memory (called Transient Buffer Board, TBB) is used that can store 5 s of data per antenna. Upon an external trigger, taken from lightningmaps.org (n.d.), the data on the TBBs are frozen and read out for later processing. This system can typically distribute a trigger signal to the LOFAR stations within a second of the lightning flash, so that the majority of recorded lightning flashes fit within the saved data. In this read-out process, we experience some data loss (due to missed hand-shaking during the download from the antenna field) which, thanks to our large number of antennas, does not affect the image quality. Per 5 s recording we store close to 1 TB of data for later off-line processing. The antennas have been calibrated on the galactic background radiation (Mulrey et al., 2019).

2.2. Locating VHF Sources

The basis of our VHF source locating procedure is described in Hare et al. (2019). We choose a reference antenna which usually is located in the core at the Superterp. For each pulse that we want to locate we select a relatively small section of the time trace in the reference antenna. The arrival times of pulses from this source at other antennas are calculated from the cross-correlation of the selected trace with the traces in the other antennas. The source position is determined from a chi-square fit of these arrival times.

Imaging a flash starts with RFI mitigation, see Section. 2.2.1. The time calibration of all participating antennas, discussed in Section. 2.2.2 is the step that requires most attention since we want to reach an accuracy of 1 ns for all antennas. Finding the source positions is the third step which is through a fully automated pipeline, see Section. 2.2.3. For the final image, we select those sources that obey certain quality conditions, see Section. 2.2.4, where one has to balance keeping a sufficient number of sources with limiting the scatter. Full details of the new procedure are given in Scholten (2020), here we will outline the main aspects.

2.2.1. RFI Mitigation

Since the LOFAR core is situated in a rather densely populated part of the world there are many radio and TV transmitters that interfere with our observations. Because of these our frequency range is limited to 30–80 MHz. At lower and higher frequencies there is too much RFI to excise it. The few narrow-frequency lines in our detection window we mitigate by software notch filters. Since these notch filters eliminate a minor fraction of the frequency band (about 0.1%) this does not distort the signal, as has been checked.

2.2.2. Timing Calibration

Since we want to achieve meter-scale resolution the relative timing of the antennas has to be calibrated at the nanosecond level. To achieve this over distances of 100 km, we use a few selected pulses emitted during the flash in a bootstrap procedure. Regularly spread over the duration of the flash a small number (order of five) of blocks of data (one block is 32k of 5-ns time samples, about 0.16 ms) are taken for the reference antenna, which is taken in the dense core of LOFAR on the Superterp.

Here, and later in the imaging procedure, we minimize, using a Levenberg-Marquardt algorithm (Dennis et al., 1981), the root mean square time difference between the calculated and measured arrival time differences (RMS_d) for all antennas to find the position of a source. The calculation uses the travel time of a signal from the source to the antenna. The measured arrival time differences are obtained from the timing of the peak in the absolute value of the cross-correlation between a small section around the pulse in the reference antenna and the spectrum in the other antennas. For the reference antenna this section is 20 samples (100 ns) long, chosen to be a bit larger than the typical pulse response of the system. This is padded with zeros to match the length of the section in the other antennas which is typically taken to be 160 samples (800 ns) to make it conveniently larger than the actual search window discussed in the following section.

In each block, up to the four strongest pulses are identified as candidate calibration pulses. The pulses from the same candidate sources are selected in the nearby stations. A candidate is eliminated from the calibration procedure if there is an ambiguity in selecting the correct pulse in the adjacent antennas. The known LOFAR timing calibrations are sufficient at this stage which for the core has an accuracy better than 5 ns. The RMS_d is minimized to find the locations of the candidate calibration sources. The Dutch antennas are separated in rings with increasing diameter. In iterations that follow, a larger ring of antennas is included. For each iteration the source locations found in the previous iteration is used to make an educated guess of the pulse timings for all antennas from these calibration sources. In a chi-square fit, the optimal station timing calibrations (the same for all pulses) are determined while at the same time updating the source locations. A station is excluded from the procedure for a particular calibration source when the pulses attributed to this source show a large difference with the actual arrival times for all antennas in this station. In the calculation of the pulse arrival time, an average index of refraction, $n = 1 + 3 \times 10^{-4}$, is taken into account. Local differences, possibly due to variations in air temperature or humidity, which are small, are absorbed in the calibration constants as they vary over long distance and time scales.

The fitting procedure is repeated increasing the radius of the ring around the reference antenna until all stations are included. Frequent visual inspection of the cross-correlation spectra is important to guarantee that the used pulses are correctly assigned to the correct calibration source. When there is doubt, the candidate calibration source is eliminated from the procedure.

In the final stage, the antennas in each station are calibrated (allowing for differences between antennas in the same station) by fitting simultaneously the antenna timings as well as the source locations of the remaining high-quality calibration sources, taking the previously obtained results as an initial guess. At this point, we reach a combined RMS_d (between calculated and measured time differences) of 1–2 ns (may differ for different flashes) for about 15 sources distributed over a flash. Note that each remote LOFAR station has an atomic clock for timing stability (van Haarlem et al., 2013).

2.2.3. Source Finding

The general source-finding stage is usually run as a standalone process. This is in contrast to the calibration stage, which requires human inspection. The time trace for the whole flash is divided into overlapping blocks (32k of 5-ns time samples, with 7,000 samples overlap) for each antenna and further processing is done on each block. The overlap is chosen such that the pulses from sources anywhere in the general area of the flash can be recovered in all antennas which is checked inside the program. The position of the sources is determined in a cartesian coordinate system centered at the LOFAR core. Here, N, E, h label North, East, height (vertical distance), respectively, as defined at the core which differs slightly from those at the position of the flash.

The block of the reference antenna is searched for candidate pulses to be located. The overlap regions are excluded so that the same source is not located twice. Candidate pulses are the strongest ones that differ in peak position by more than at least 100 ns (more for very broad pulses) in the reference antenna and are seen in the two antenna polarizations (dual polarization). Within each block the candidate pulses are ordered in decreasing peak amplitude.

For each candidate pulse in the reference antenna, a section of the time trace around the pulse is taken for the calculation of the cross-correlation with other antennas, following the same procedure as discussed in the previous section. Source finding starts by performing a grid search over source locations for minimizing the RMS_d of the difference between measured and calculated time differences for antennas on the Superterp. The thus obtained source location is taken as the initial guess for a chi-square search to find the optimal source location by minimizing the RMS_d for all antennas within a certain distance from the core.

This fitting is repeated for an increasing number of antennas by increasing the circle of included antennas. Peaks in the cross-correlations are searched for within a timing window. The timing window is calculated for each antenna as the maximal change in arrival time of the pulse when the source is moved within the volume defined by the covariance matrix that was obtained from the previous chi-square fit (i.e., contracting the covariance matrix with the Jacobian, the derivative of the arrival time w.r.t. source position) and adding an additional 10 ns. The window is implemented as a “soft” window by multiplying the absolute value of the

(complex) cross-correlation by a parabola, with the corresponding width, before determining the timing of the peak, the maximum. If the peak in the cross-correlation deviates by more than two standard deviations the antenna is flagged as excluded from the fit. An antenna is also excluded when the width of the cross-correlation, defined as the integral divided by the peak value, differs by $>60\%$ from that of the self-correlation in the reference antenna. The reason for excluding antennas is that it may happen that two pulses are close, or even interfere, for a particular antenna. It may also happen that the pulse is “hidden” in the noise. Not capturing this may derail the search for the source location.

The procedure of finding the source, by gradually including more antennas while limiting the search window, is inspired by that of the Kalman filter. It is, however, more accurate than even the extended Kalman filter since it does not involve a linearization approximation. See Pel (2019) for an implementation of the extended Kalman filter for lightning imaging.

After finding the source location the corresponding samples in the signal trace of each antenna is set to zero and the following candidate pulse is taken.

The inverted V-shaped LOFAR antennas have two possible orientations, SW-NE and SE-NW, and are thus sensitive to different polarizations of the incoming radiation. We notice that the pulse-shape may differ for the two polarizations, see Section 3.1.3 for an example. For this reason, we have organized our imaging algorithm such that it is an optional choice if only one of the antenna polarizations or both are used in imaging where dual (both) is the default. In general, there is little difference in the image quality for the different options. Using only one of the antenna polarizations usually gives a larger number of good quality sources; however, this may introduce a bias in the image.

2.2.4. Source Quality

We observe that the location accuracy of a source is poorly reflected by the covariance matrix that is obtained from minimizing the RMS_d . The reason is that selecting a wrong pulse in a series of antennas may still yield a reasonable fit but will result in a source that is mislocated. We have observed that the obtained value for the RMS_d combined with the number of excluded antennas, N_{ex} (the lower this number the better), appear to be good additional indicators of the location accuracy, supplementing the diagonal element of the covariance matrix corresponding to the error on the height, $\sigma(h)^2$, which is usually the largest.

Antennas are excluded from the fitting procedure when there is no clear peak in the part of the spectrum that was searched. This could be due to the fact that the pulse is simply too weak to be seen but it could also be that the peak lies outside the search window. The latter is obviously problematic and should have contributed to RMS_d . The setting of the location quality indicators ($\sigma(h)$, RMS_d , and N_{ex}) is dependent on the location of the flash with respect to the core. Additionally, the criteria tend to be subjective, balancing a large number of sources with a minimum of mislocated sources. In many cases, the mislocated sources appear to be displaced by 50 m or more along the radial direction with the core of LOFAR at the center.

2.3. Broadband Measurements with a Magnetic Loop Antenna

In September 2018, the broadband magnetic loop antenna SLAVIA (Shielded Loop Antenna with a Versatile Integrated Amplifier) (Kolmašová et al., 2018) has been installed by the Department of Space Physics, Institute of Atmospheric Physics of the Czech Academy of Sciences at a site about 10 km east from the LOFAR core near the village Ter Wisch, marked with the red \odot in Figure 1. The antenna has a surface area of 0.23 m^2 and measures the time derivative of the magnetic field. The obtained waveforms are then numerically integrated. The sampling frequency is 200 MHz, the frequency band is limited by a first order high-pass filter at 4.8 kHz and by a 13th order low-pass filter at 90 MHz. The sensitivity of the recording system is $6 \text{ nT/s}/\sqrt{\text{Hz}}$ corresponding to $1 \text{ fT}/\sqrt{\text{Hz}}$ at 1 MHz. At the Ter Wisch site, the signal is unfortunately affected by strong man-made interferences, some of which cut through our high-pass filter, and the waveform had to be cleaned by 19 narrow band-rejection filters with bandwidths 18–30 Hz at interference frequencies between 2 and 10 kHz, and at 18 kHz.

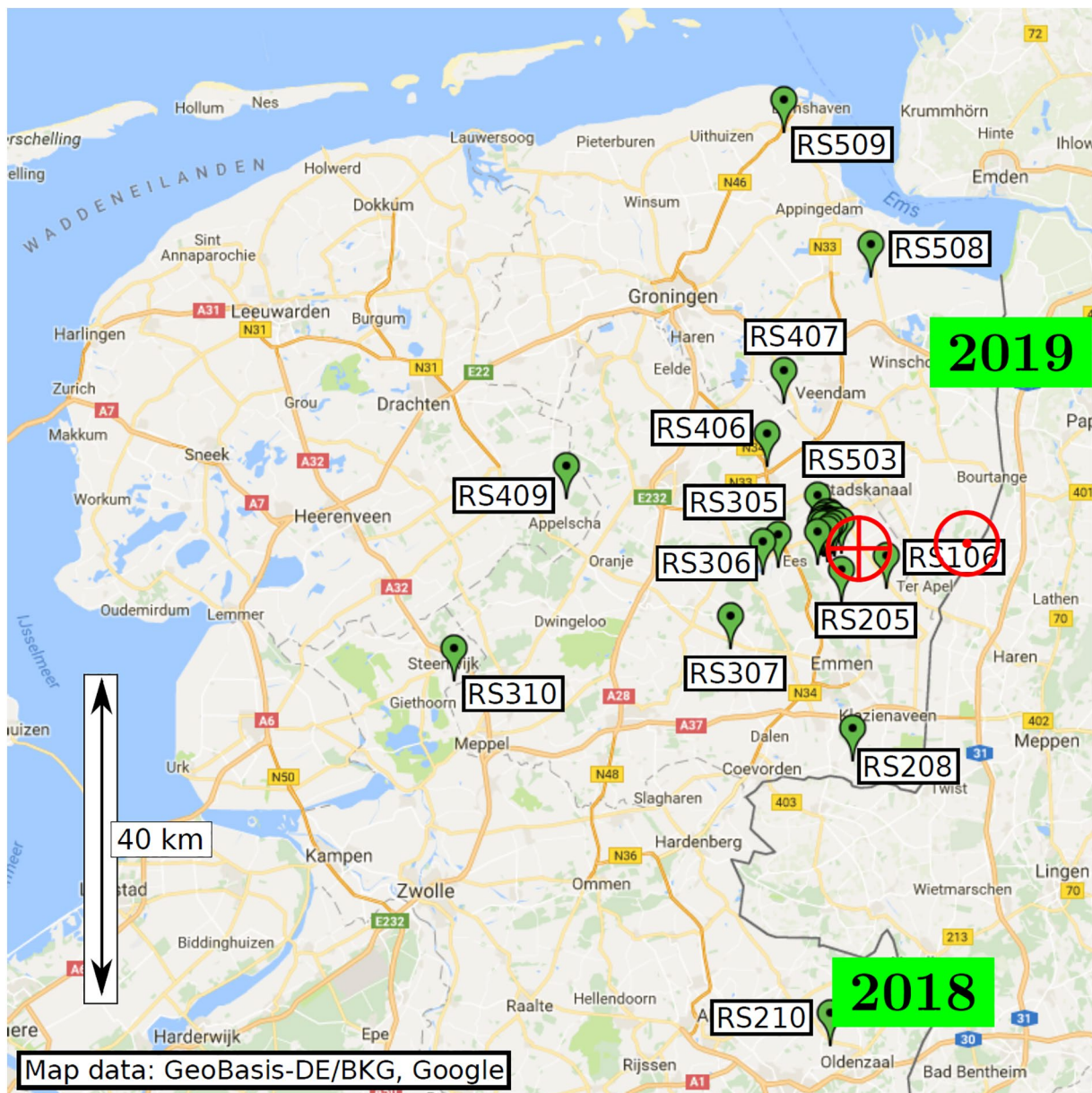


Figure 1. Layout of the Dutch LOFAR stations, adapted from Hare et al. (2018). The core of LOFAR is indicated by the red \oplus sign and the positions of the Dutch remote by the green markers labeled by their number. The position of the broadband magnetic loop antenna SLAVIA is indicated by the red \odot . The green boxes show the general location of the 2018 and 2019 flashes that are discussed in this work.

3. The Initial Stages of Dutch Lightning Flashes

In this work, we concentrate on imaging the initial development of two lightning flashes, where we selected one from 2018 and another one from 2019. The 2018 flash shows features we see in all our imaged flashes (about 10 in total). A PIL is initiated at the lower side of a negative charge layer. This initial leader propagates with a velocity of about 10^6 m/s downward to the positive charge layer. There it simultaneously initiates many negative leaders of which one or two continue to propagate over large distances. The 2019 flash shows a more complicated pattern which can be understood as a PIL initiating, in the usual way, several negative leaders. Two of these convert into an initial leader again after a few milliseconds. This second generation of initial leaders we have named secondary initial leaders. In Section 3.2, we will also present data for the 2019 flash from a broadband magnetic loop antenna (Kolmašová et al., 2018).

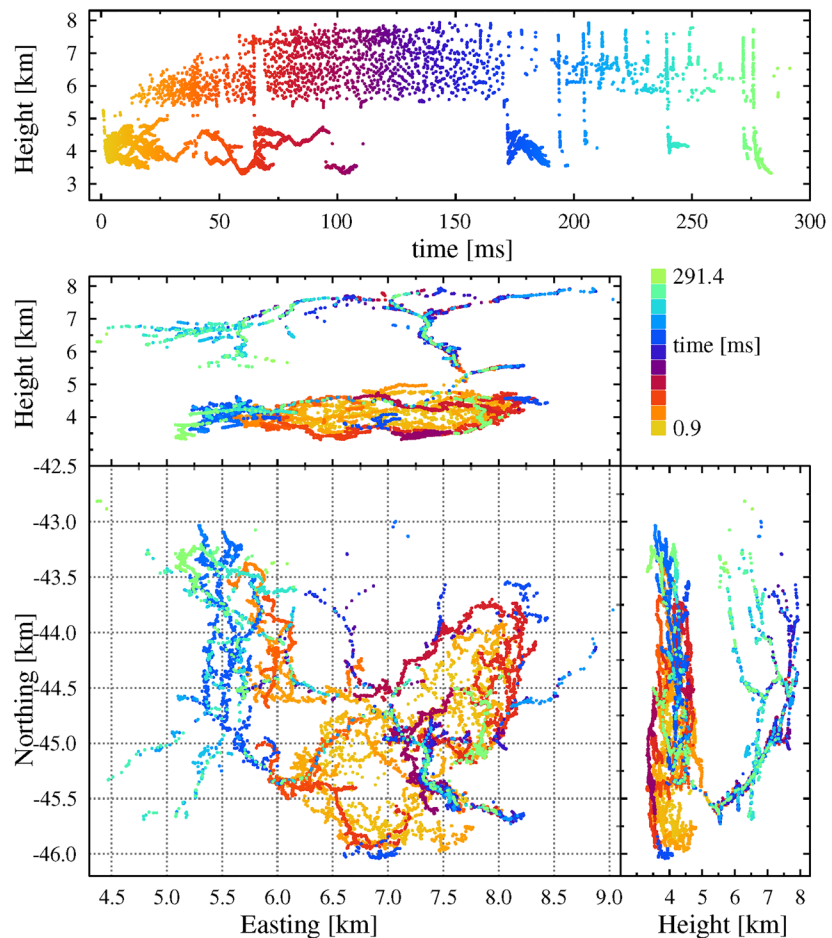


Figure 2. Image of the 2018 flash showing sources with $\sigma(h) < 3.5$ m, $RMS_d < 3$ ns, and $N_{ex} < 10$ resulting in 14,267 located sources. The top panel shows height vs. time of the sources where we have applied an offset to put initiation close to $t = 0$. The same sources, with the same coloring, are shown in the other panels giving height and distances north and east from the LOFAR core.

3.1. The 2018 Flash

The complete 2018 flash, shown in Figure 2, is a typical example of a flash imaged with our techniques. The lightning flash occurred on August 13, 2018 at 15:30 at a distance of about 50 km from the core of LOFAR, see Figure 1. To obtain this image, we have used antennas for both polarizations and set the limits on the source quality as $\sigma(h) < 3.5$ m, $RMS_d < 3$ ns, and $N_{ex} < 10$ from a total of about 265 antennas. This leaves 14,267 located sources over the whole duration of the flash of 0.3 s. To give some idea of the effect of these limits, we have relaxed the limit on the RMS_d to $RMS_d < 4$ ns which yields an image with an estimated 100 sources that are mislocated by about 100 m out of a total of 23,606. Since the first located pulse of a flash is dependent on the applied source quality criteria we have not performed any fine-tuning in determining the time offset for Figure 2.

The flash shown in Figure 2 has a typical structure of flashes we have seen over the LOFAR area. The flash initiates at an altitude of about 5 km at the bottom part of the negative charge layer to develop first a PIL that triggers a number of negative leaders in the lower lying positive charge region. These charge layers are inferred from the location of the positive and negative leaders seen later during the flash (Dwyer & Uman, 2014; Shao & Krehbiel, 1996). Only after about 20 ms the positive leader becomes visible in the form of increasing twinkle activity as we have reported in Hare et al. (2019) for a different flash. The PIL forms a plasma channel that continues to serve as the link between the upper negative and lower positive charge layers and called the “neck” in this work. The initial leader we observe is reminiscent of what is reported

on in, e.g., Lyu et al. (2016) to occur at the initial phase of lightning storms in the United States with the main difference that there the positive charge layer is positioned above the negative one. This difference is often referred to as normal (positive charge over negative) and inverted (negative over positive) IC flashes (Bruning et al., 2014). However, absence of upward negative leaders does not exclude the possibility that also Dutch thunderstorms have the usual tripolar structure seen in most United States thunderstorms with a lower positive, middle negative, and upper positive charge layer. Such a structure is in fact supported by the work reported in Trinh et al. (2020).

3.1.1. The Initial Development

To visualize the dynamics of the leader development after initiation, Figure 3 shows the time development in chronological frames. Time frame A shows the PIL starting at an initial height of 5.25 km developing downward. For the first 0.5 ms, no progression is observed but then it accelerates and progresses downward

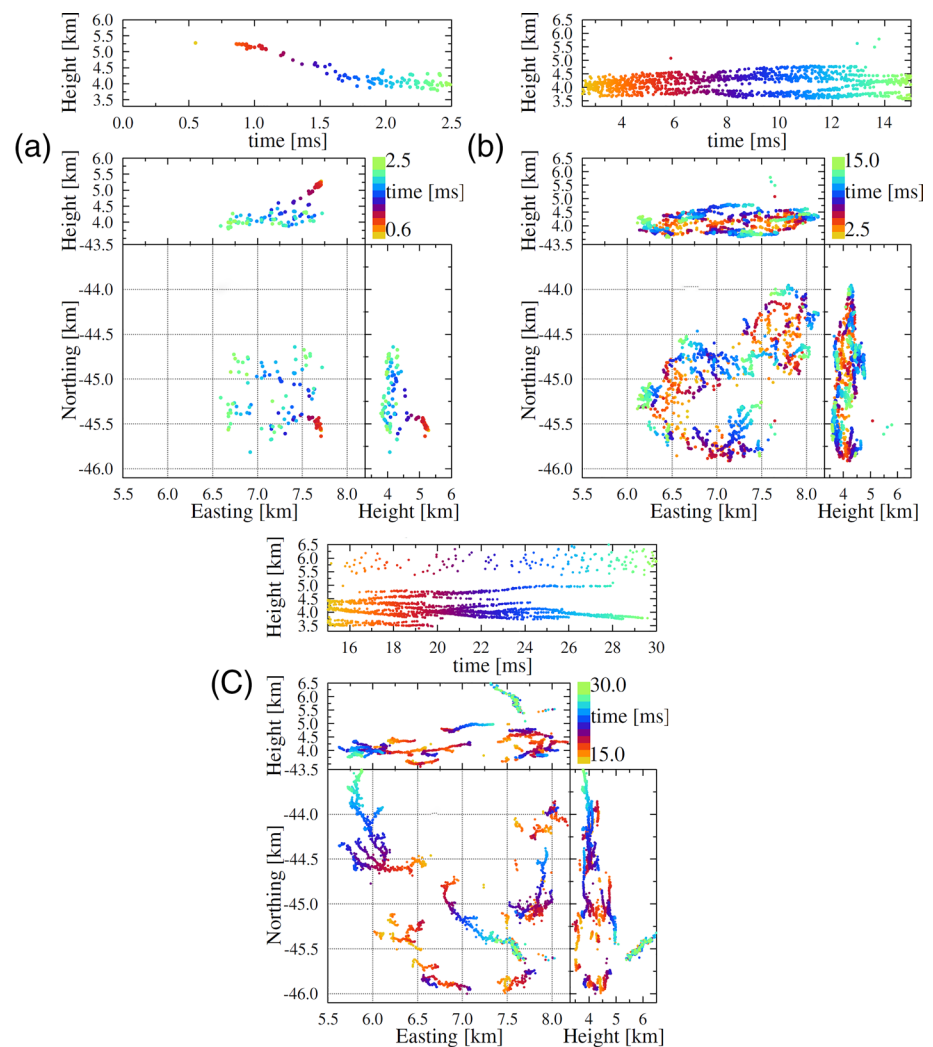


Figure 3. The early part of the 2018 flash is imaged for three subsequent time periods to emphasize the dynamics in the initial stage. Shown are sources with $\sigma(h) < 3.5$ m, $RMS_d < 4$ ns, and $N_{ex} < 20$ resulting in 113, 2,849, and 2,814 located sources, respectively, for the three different time frames. After initiation at a height of 5.2 km one observes a fast downward progression (a). At a height of about 4 km, the downward motion stops and negative leaders develop in seemingly arbitrary directions at multiple places over an area in excess of 1 km² (b). At the end only one continues to grow (c). Three time frames, not panels; figures need some work, we could show also subsequent time frames.

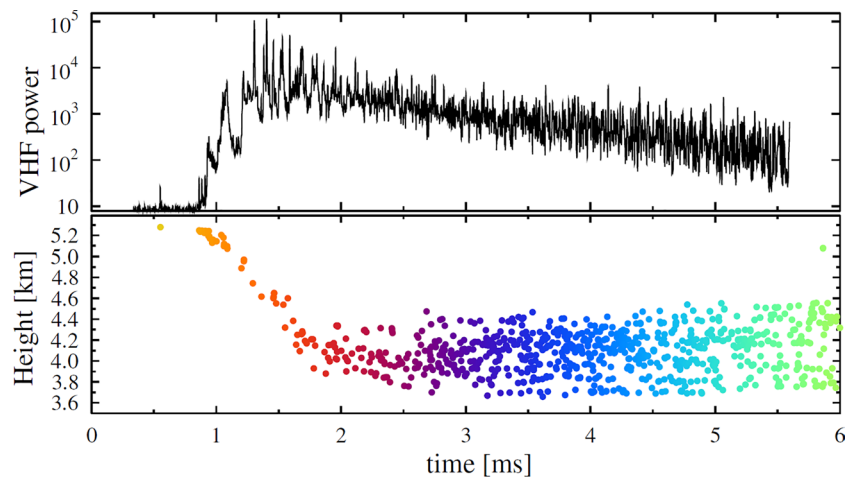


Figure 4. The VHF power in arbitrary units in 4 μ s bins is compared to located sources for the first 6 ms of the 2018 flash.

along a slanted path at about 1.2×10^6 m/s, somewhat faster than observed in Lyu et al. (2016). After a kink in the path at 5-km altitude (visible most clearly in the north vs. altitude plot), the PIL fans out, initiating a multitude of negative leaders at an altitude of about 4.5–4.0 km where the downward motion stops (see time frames B and C). Then distinct, almost horizontal, leaders develop in the same fashion as negative leaders do with a speed of about 10^5 m/s, i.e., 10 times slower than the initial leader. It is impressive that the formation of negative leaders starts simultaneously at multiple places over an area in excess of 1 km^2 (b). Each of the new leaders appears to develop in seemingly arbitrary directions, some inward, some outward. Close inspection shows that they rather seem to cover the surface of a spatial structure. One also notices that there is some VHF activity along the path of the initial leader at 6 and 8 ms and 5.2–5.3-km height. Since this particular region in space is observed to play a rather special role in the evolution of the flash we named it the neck. The observed VHF emission indicates that current is flowing through the neck, even though there is no observed activity of a positive leader yet. Only after 13 ms the positive leader starts to show at an angle w.r.t. the PIL. The neck will serve as the connection point between the upper negative and the lower positive charge for the whole duration of the flash. Time frame C shows a pronounced positive leader with ample twinkling activity along several needles (Hare et al., 2019; Pu & Cummer, 2019). The neck itself shows no needle activity. It is interesting to see that one negative leader propagated to within 500-m horizontal distance and at the same altitude of the place where the neck showed a kink and started to fan out. Eventually there is only a single negative leader (in the top left corner of the plan view) that continues to spread away from the initiation point, all others appear to have stalled.

3.1.2. The Primary Initial Leader

Figure 4 shows the PIL with the located sources together and the recorded power. The power is calculated as the square of the measured VHF-signal from on one of LOFAR's core antennas and averaged over 4 μ s. It is interesting to see that the VHF activity increases rapidly after initiation, reaching a peak at the time the initial leader creates a multitude of more normal negative leaders. This takes place 2 ms after initiation. At later times, the VHF activity decreases again.

Making use of our high resolution, Figure 5 shows a zoom in of the initial leader to provide a better look at its properties. From the very first source, marked with a star, the initial leader appears to fan out extending to about 100 m in height and less in horizontal directions. In the first part of the initial leader development, a few different stages can be distinguished. The first stage ranges from initiation, $t = 0.55$ ms, until $t = 0.94$ ms. The VHF trace shows almost no power above background. The imager finds several good quality sources toward the end of this period. At this first stage, the leader moves over a distance of 20-m horizontally and 50 m downward at a speed of 1.3×10^5 m/s. In the subsequent second stage, lasting from $t = 0.94$ to 0.97 ms, increased VHF activity is visible. During this stage, the leader moves over a distance

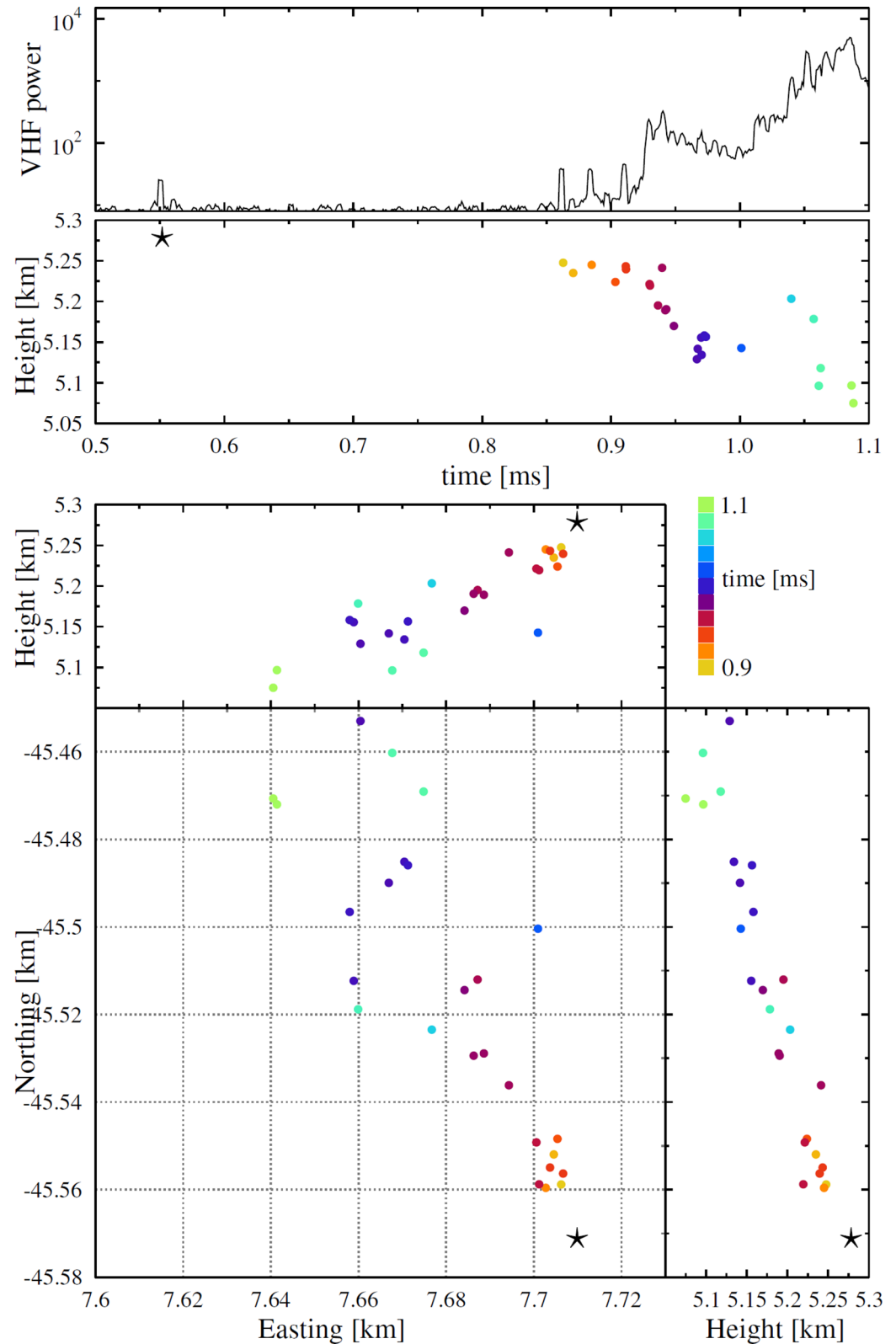


Figure 5. A zoom in on the sources observed in the initial 1.1 ms of the 2018 flash. The first located source, the initiation point, is marked with a black star.

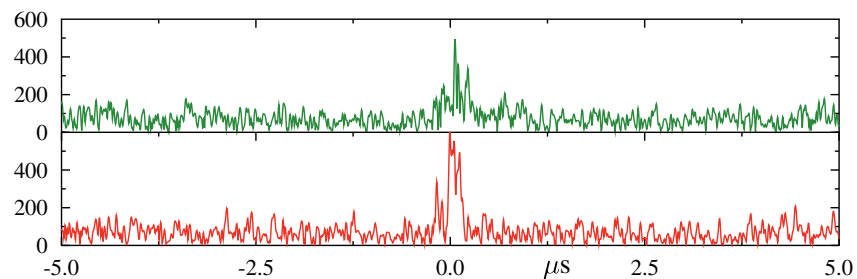


Figure 6. The Hilbert-envelope of the trace for each of the two polarization directions as measured at the core of LOFAR. The vertical axis gives pulse amplitude in arbitrary units, the horizontal axis time (in μs) centered at the first located source (at 0.55 ms in Figure 5).

of 80-m horizontally and 90 m downward with a speed of 4×10^6 m/s, considerably faster than in the first stage. The third phase lasts till about 1.1 ms where one sees a clear second burst of VHF intensity. The few sources (6) that are located at this stage are lying on a continuation of the leader seen at the second stage or around the previous leader. In the fourth stage from $t = 1.1$ to 1.8 ms, the initial leader continues to propagate down and continues to fan out. The few sources we locate in the interval from 1.5 to 1.8 ms are spread over a slanted disk with a size of about 300 m in north-south as well as east-west as can be seen in panel a of Figure 3. At this stage, the VHF emission reaches a maximum and the high density of pulses prevents us from performing efficient source localization. In this stage, the speed is about 2×10^6 m/s. At later stages, the general downward motion stops, the propagation speed decreases, the VHF intensity continues to drop, and we are able to locate an increasing number of sources. From the located sources, we observe that a multitude of negative leaders branch off from the PIL, and then propagate at the typical speed of a negative leader, 10^5 m/s.

3.1.3. Initiation Pulse

To show that the flash activity already started at 0.55 ms, we show in Figure 6 a part of time trace in the vicinity of this first located source. Here, the pulse stands out clearly and, because the spectrum is relatively clean, we can observe it in all antennas. Also, some even smaller pulses can be located, but these do not pass the quality criteria used in making Figures 3 and 5. It should be noted that the trace in the two polarization directions is rather different, see Figure 6, signaling that this first located pulse is due to a complicated current pattern, with currents in multiple directions. In addition, this pulse is considerably longer than the pulse response of our system (which is 50 ns FWHM) which is additional evidence that its source is composite, not just a single short pulse. We observe that the substructure of the pulse does not change significantly for antennas at different orientations w.r.t. the source (taking into account the polarization). Based on the pulse response of the system of 50 ns (15-m length at the speed of light), we thus conclude that the spatial extent of the source must be small, of the order or less than $(10 \text{ m})^3$. While the duration and polarization of the RF signal implies that the structure of the current is complex, the VHF emission is also very impulsive. We have compared the arrival times of the different peaks between antennas that are far-apart and on opposite sides of the source region. We have found that the relative peak times changes < 50 ns between the different antennas, implying that the source region is small. As, if the source region was large, the relative times between the different VHF peaks should change between antennas that are far-apart.

3.2. The 2019 Flash

The complete image of the 2019 flash we discuss in this paper occurring on April 24, 2019 at 21:30 UTC is shown in Figure 7. To have a not too high density of sources we show only those with $\sigma(h) < 3.5$ m, $\text{RMS}_d < 3$ ns, and $N_{\text{ex}} < 25$ (out of a total of close to 400), leaving a total of 46,523. The time is shifted such that the flash starts close to $t = 0$. For this flash, we could locate a larger number of sources per ms than for the 2018 flash, probably because it is closer to the LOFAR core. The flash shows the same charge-layer structure as was seen for the 2018 flash discussed in the previous section. For this flash, the positive charge

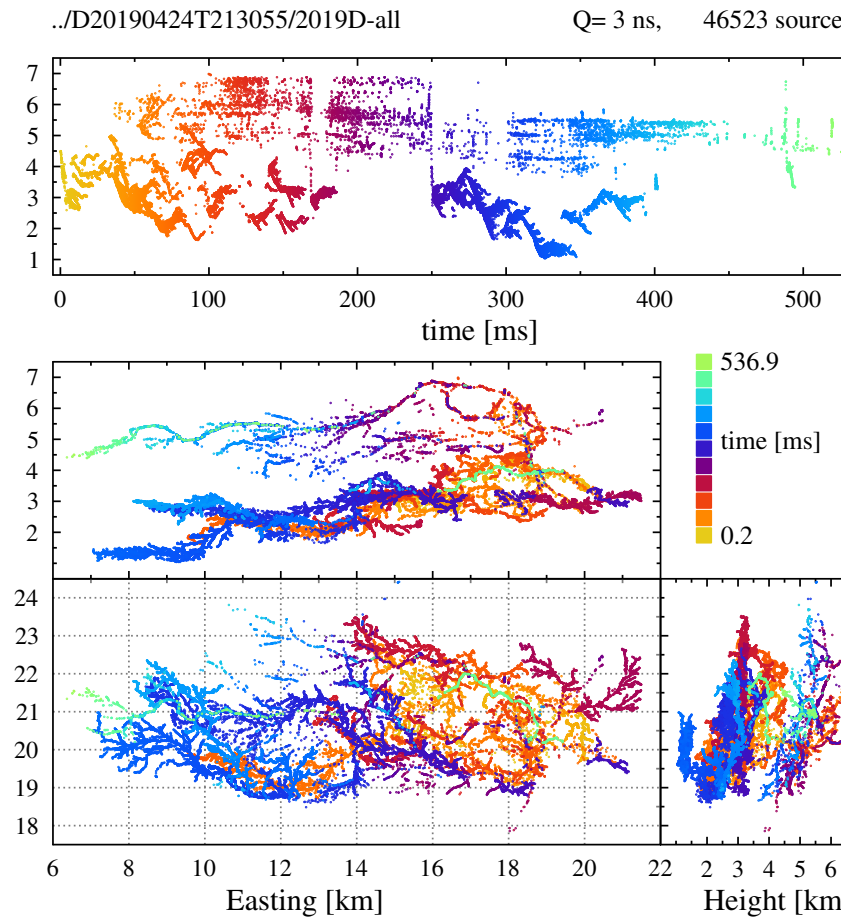


Figure 7. Image of the 2019 flash showing sources with $\sigma(h) < 3.5$ m, $RMS_d < 3$ ns, and $N_{ex} < 25$ (out of a total of close to 400) are shown, resulting in 46,523 located sources.

layer extends from about 4 km almost to the ground. The negative charge layer does not extend above 7 km height. These heights have been inferred from the heights of the positive and negative leaders. The currents from the lower positive to the upper negative layer all appear to flow through the neck that was formed at initiation. In Section 3.2.2, we will show that within 100 m from the neck we observed a negative leader propagating to the positive charge layer.

3.2.1. Secondary Initial Leaders

The initiation phase of the 2019 event is shown in detail in Figure 8. To improve the image quality, we relaxed the conditions on the sources slightly over those applied in Figure 7, $\sigma(h) < 3.5$ m, $RMS_d < 5$ ns, and $N_{ex} < 35$ leaving 32,399,413, and 2,332 sources respectively in panels A ... D. It has been verified that there is no distinct peak visible in the time traces before the time of the first located source at $t = 0.1$ ms. For Figure 8, we have relaxed the condition on the source quality a little, setting $RMS_d < 5$ ns and $N_{ex} < 35$, to increase the number of located sources, and made sure that the cuts were such that there were no obviously mislocated sources. Time frame A in Figure 8 shows that after initiation the PI propagates downward in an accelerated motion reaching a speed of about 2×10^6 m/s rather straight down this time. At an altitude of about 4 km, it starts to fan out, producing a multitude of negative leaders over an area of about 1 km^2 . This is qualitatively the same as was observed for the 2018 event. Time frame B shows that after 3 ms most of the negative leaders stop propagating, while two of them show a fast motion covering a distance of 2 km in 2 ms, 10 times faster than the propagation speed of normal negative leaders (10^5 m/s) and the same as that of the PIL. Another resemblance is that the number of located sources on this leader is relatively low.

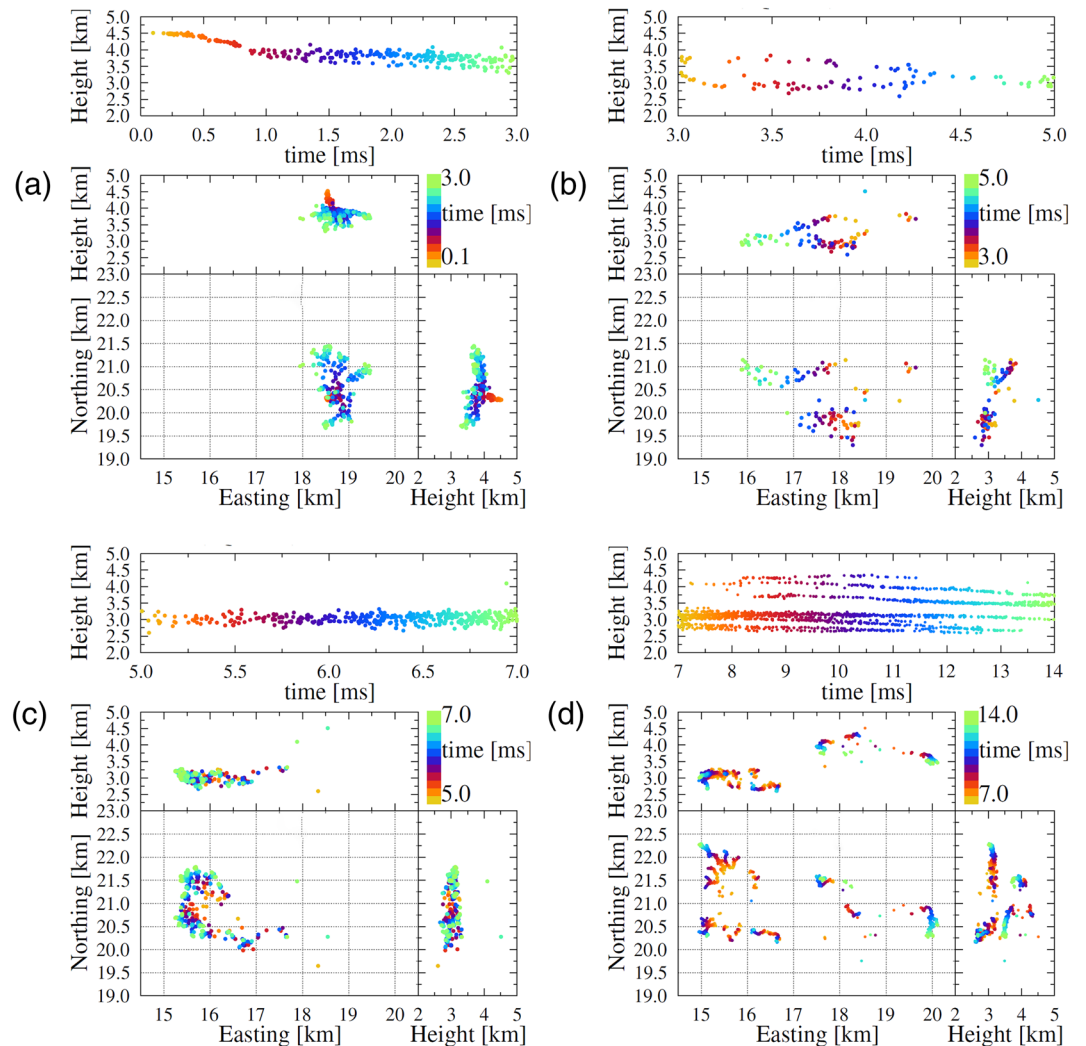


Figure 8. The initiation of the 2019 flash. Setting the location quality at $\sigma(h) < 3.5$ m, $RMS_d < 5$ ns, and $N_{ex} < 35$ leaves 32,399,413, and 2,332 sources for the different sequential time frames. The black star in time frames (b) D marks the position of the point of initiation.

For this reason, we call them secondary initial leaders. The bottom-left panel shows that when they reach a height of 3 km one of the secondary initial leaders repeats the process of generating a multitude of negative leaders over an area in excess of 1 km^2 , i.e., in the same positive charge layer situated a kilometer below and 2 km eastward than from the positive layer seen in time frame A. The bottom-right panel shows that most of the negative leaders in the second phase have stopped propagating, and that some of the initial group are reactivated.

At the time of initiation of this flash the magnetic loop antenna recorded data. The magnetic loop antenna is situated at a site some 10 km east from the LOFAR core, see Figure 1. Figure 9 shows the recorded magnetic loop antenna spectrum aligned with the located sources and the VHF power (averaged over $2 \mu\text{s}$) as recorded by LOFAR. The figure shows that during the evolution of the PIL, in the first 1.5 ms, the VHF power increases in steps, identical to what was observed in Figure 5 for the 2018 flash. During this time, the magnetic loop antenna recorded a dozen strong initial breakdown pulses. The VHF power shows another strong increase (by a factor 2 or 3) at $t = 3$ ms when the secondary initial leaders start to emerge. Around the same time the magnetic loop antenna also measures an enhanced density of initial breakdown pulses. There is another phase of enhanced activity seen in the magnetic loop antenna when the secondary initial leaders initiate the negative leaders around $t = 4.5$ ms. At later times there is a gradu-

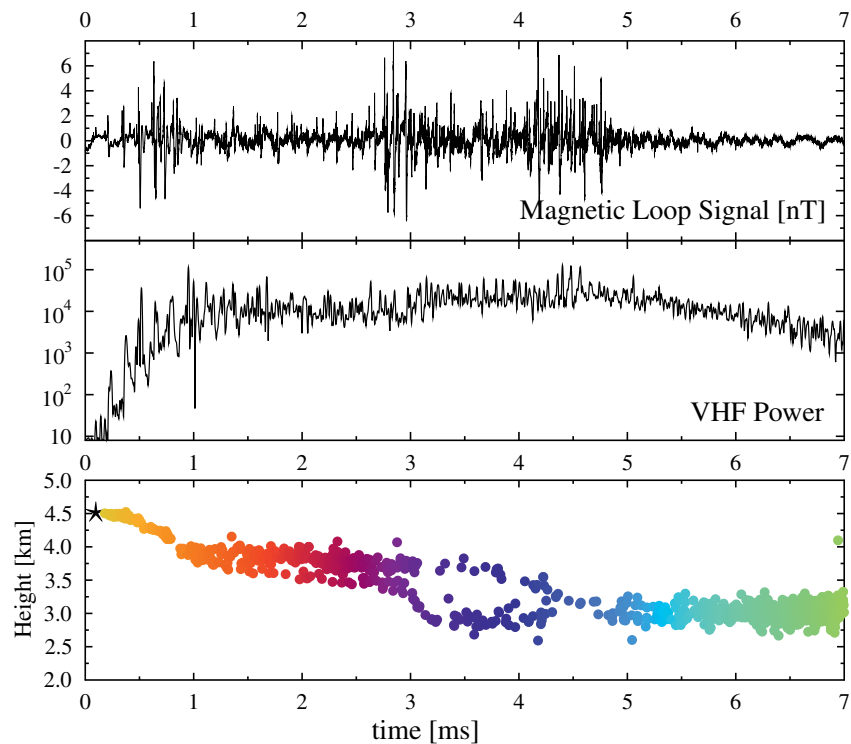


Figure 9. The power recorded at a core station of LOFAR (rebinned over $2\ \mu\text{s}$, middle panel) is compared to the recording in the magnetic loop antenna (top panel, units of [nT]) and the height of the located sources shown for the first 7 ms in Figure 8. All panels have been aligned in time.

al drop in the VHF power, at about the same rate as seen for the 2018 flash, of about 1 order of magnitude over 2 ms.

Figure 9 also suggests that while the PIL is more gradually accelerated, the SIL moves immediately at the top speed, one straight down, the other initially horizontal. This can be read from the figure by the parabolic downward slope in the height vs. time panel for the PIL while the SIL follow a more straight downward slope.

Zooming in on the first millisecond of the flash, Figure 10 shows many interesting aspects of the PIL of which we mention here only a few.

The broadband spectrum shows several pulses, each of which occurs at about the same time a burst is seen in VHF power. This VHF emission is in the form of an enormous number of small pulses that combine in a strong increase in the emitted power. The full width at half maximum of such a burst, as can be determined from the first one, is about 0.01–0.02 ms. This is very close to the burst duration seen in Hare et al. (2020) where it is associated with negative leader stepping. However, the time between bursts of VHF power is about 0.1–0.15 ms which is longer than the 0.05 ms observed in Hare et al. (2020) for normal negative leader propagation. Negative leaders at heights between 2 and 4 km were analyzed and no dependence on altitude was observed over this range.

From Figure 8, it can be seen that the initial leader propagates almost vertically downward and the propagation speed can thus be deduced directly from Figure 10. This indicates a constant acceleration of the PIL after it starts propagating, very similar to what was observed for the 2018 flash.

In a follow-up paper, (?), the correspondence between the broadband signal and the LOFAR image will be discussed in more detail. There we will address the pulses seen later during the flash, beside those seen in the broadband time trace close to initiation.

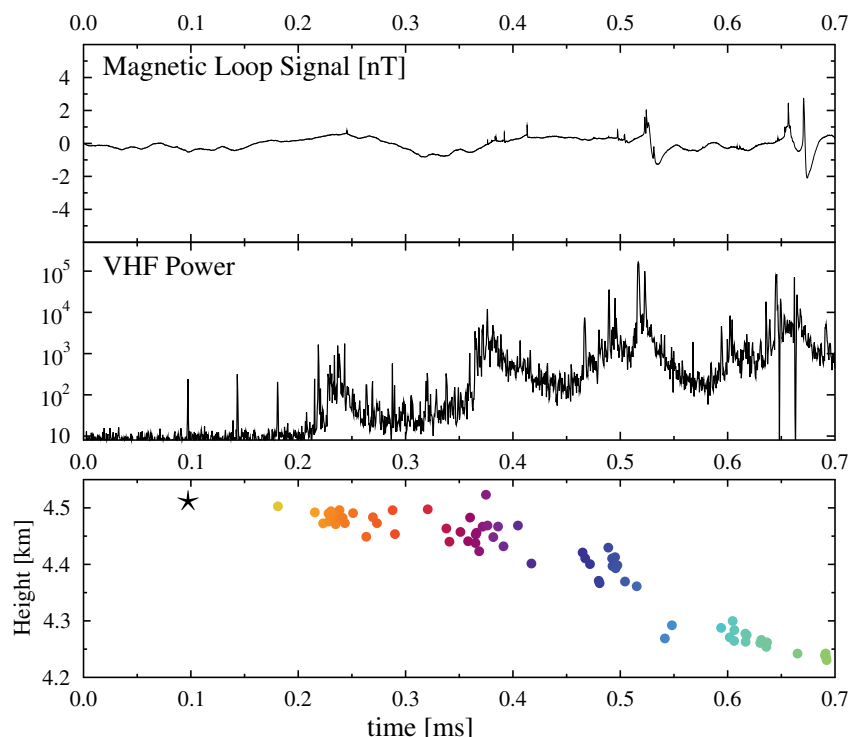


Figure 10. The power recorded at a core station of LOFAR (rebinned over $0.5 \mu\text{s}$, middle panel) is compared to the recording in the magnetic loop antenna (top panel) and the height of the located sources shown for the first 0.5 ms in Figure 8. All panels have been aligned in time.

3.2.2. The Neck Region

In the vicinity of the neck region, we have observed some interesting leader propagation that should be taken into account when reconstructing the structure of the charge layers in the vicinity of the initiation point labeled with a \bigcirc in Figure 11. At about $t = 10 \text{ ms}$, a negative leader propagates up to the point (a) in the figure, a mere 500 m away from the initiation point horizontally. At $t = 35 \text{ ms}$, the same negative leader activates a second time and approaches even to a distance of 300 m . At about the same time from point (b) at an altitude of 5 km , a negative leader starts to propagate down, with no previous activity seen at its initiation point, toward the neck, to turn parallel to it at a distance of a mere 100 m where it stops propagating at the top of the charge layer where the first negative leaders were observed. At about the same time, some VHF sources are observed along the positive leader. At $t = 55 \text{ ms}$ at (c) a bit higher than 5 km another negative leader starts propagating toward point (b) where it appears to connect to the channel of the earlier negative leader that started from here. This very complicated leader structure seems to imply that around the initiation point a fair amount of charge was present in a complicated charge structure. In the 2018 flash, we have also observed that a negative leader propagated up from the lower positive charge layer to the vicinity of the neck, but the other features appear to be unique for the 2019 flash.

4. Discussion and Conclusions

We have improved the procedure used in Hare et al. (2019) for imaging lightning flashes using data from the LOFAR radio telescope. Our new imaging procedure has a proven capability to locate over 200 sources per millisecond of flash with meter-scale accuracy.

All images of flashes we have made with LOFAR show a negative charge layer around 5 km and below this a positive charge layer which is consistent with the atmospheric electric fields over the LOFAR core as were determined in Trinh et al. (2020). We also observe an extensive structure of negative leaders in the lower

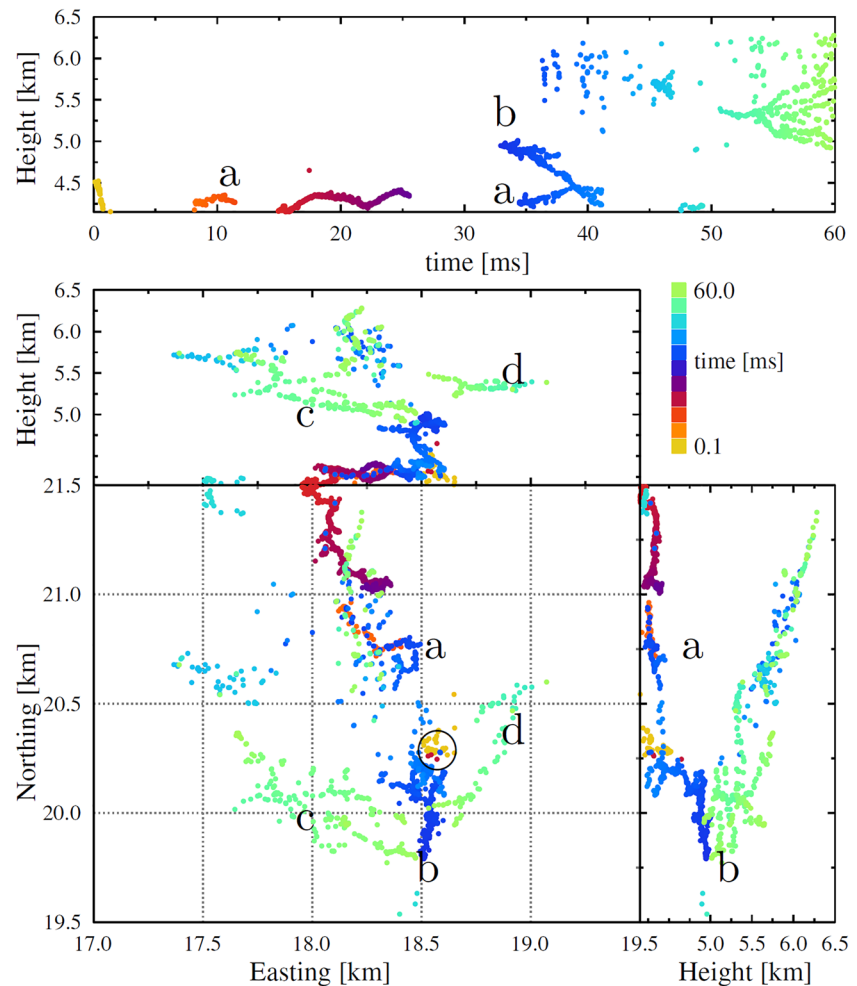


Figure 11. An expanded view of the neck region for the 2019 flash. The letters are used in the text to refer to particular parts of this image. The initiation point is labeled by the \bigcirc .

positive charge layer. Very rarely do we see negative leader activity propagating up into the upper positive layer. While for thunderstorms in the United States the IC discharges are most often observed to occur from the main negative to the *upper* positive charge layer we observe over LOFAR that the IC discharges occur between the main negative and the *lower* positive charge layers.

In all our imaged flashes, we observe a very similar initial development of the discharge where after initiation the discharge slowly grows (in fractions of a millisecond), picks up intensity (in the form of strong increase in emitted VHF power) as is typical for an initial leader. This initiation appears to happen at the bottom side of the negative charge region as inferred from the location of the positive leaders. The fact that initiation happens at the boundaries of charge regions was already reported on in Proctor (1991). When the initial leader reaches the charge pocket which attracted it, the fast forward propagation stops and instead we observe the creation of many more normal negative leaders that propagate at about one-tenth of the speed of the initial leader. It is a point of discussion (Belz et al., 2020; Tilles et al., 2019) whether the channel in this early stage of a lightning flash is a highly conducting leader or formed by poorly conducting streamers. In this work, we see evidence that this structure is well conducting, as we see evidence of large steps that produce the initial breakdown pulses, and this channel easily transitions into normal negative leaders without any new breakdown phenomena (such as recoil leaders) that would be needed to transition the region from a poorly conducting region into a well-conducting leader. Therefore, in this work, we have referred to this initial lightning propagation as a leader.

This naturally leads to the picture that the initiation at the bottom side of a negative charge layer was driven by a relatively small (order 1 km³) pocket of rather dense positive charge. This created the strong electric field that is needed to cause lightning initiation. In this strong field, the elongating leader rapidly acquires charge by induction leading to increased currents and heating which could explain the initial acceleration we observe in the PIL. An acceleration of the initial leader was also observed in Cummer et al. (2015), although the acceleration was much smaller (about a factor 2 in velocity) than what we observe (close to an order of magnitude as compared to normal negative leaders). It is interesting to note that an acceleration of leader propagation right after initiation was predicted in Behnke et al. (2005) in virgin air on the basis of a simple model. In their own observations they found instead that leaders were decelerating from which they inferred that there was preconditioning during leader initiation. Apparently, such preconditioning does not happen in our case. In the present case, the acceleration happens even faster than their prediction, even when the stepping time is taken into account (they used 1 ms while in the present case it is of order 0.15 ms). The faster acceleration might be due to a stronger ambient electric field. Since the ambient electric field extends up to the positive charge pocket, the fast propagation of the PIL stops as it reaches it and we start to observe the usual negative leaders that propagate along potential extremals (Coleman et al., 2008) and thus in a much weaker ambient field.

Our observations suggest that a relatively small positive charge pocket may be the driver for the strong electric field in which the initiation of the lightning happens. The presence of large hydrometeors (see, e.g., Dubinova et al., 2015), or a large number of small droplets (see Kostinskiy et al., 2019), will be required as initiation sites. The initiation process could be greatly facilitated by a high density of free electrons as created by cosmic rays as suggested in Rutjes et al. (2019). It is not clear if any of these mechanisms can explain the initial accelerating propagation of the initial leader that we have observed.

Most interestingly, we see in one of the two flashes studied in this work that the structure of the initial leader is repeated a few milliseconds after initiation by two SIL's. Even though they are initiated at two different locations more than a kilometer apart, they appear to propagate to the same charge pocket.

The large number of negative leaders in a very confined space, as initiated by the PIL, are a strong indication that there must have been a pocket with a rather high charge density. Once the charge in this confined charge cloud is collected the majority of the leaders stop propagating and only few remain. For the 2019 flash, there may have been another positive charge cloud in the vicinity that attracts a secondary initial leader. As this is initiated from the tip of a propagating negative leader, there is sufficient charge available to immediately have a fast-propagating discharge.

It has been suggested that turbulence is a very efficient mechanism, especially in thunderclouds for creating regions with large fields that even grow exponentially with time (Mareev & Dementyeva, 2017). This could thus be the mechanism that created the relatively small pocket with high charge density.

Another indication of a dense and complicated charge-layer structure in the vicinity of the initiation point is the fact that in our images we see a negative leader turning back toward the Neck, the initiation point of the flash. This happened for the 2018 as well as for the 2019 flash.

We observe a strong correlation between the signal of the broadband antenna and the emitted VHF power, as was already suggested in Kolmašová et al. (2018, 2019). After submission of the present manuscript, we became aware of the work of Belz et al. (2020) where a very similar structure is discussed as the PIL, this in relation to observed TGF emission.

Data Availability Statement

This paper is based on data obtained with the International LOFAR Telescope (ILT). LOFAR (van Haarlem et al., 2013) is the low-frequency array designed and constructed by ASTRON. It has observing, data processing, and data storage facilities in several countries, that are owned by various parties (each with their own funding sources), and that are collectively operated by the ILT foundation under a joint scientific policy. The ILT resources have benefited from the following recent major funding sources: CNRS-INSU, Observatoire de Paris and Université d'Orléans, France; BMBF, MIWF-NRW, MPG, Germany; Science Foundation Ire-

land (SFI), Department of Business, Enterprise, and Innovation (DBEI), Ireland; NWO, The Netherlands; The Science and Technology Facilities Council, UK.

The data are available from the LOFAR Long Term Archive (for access see ASTRON (2020)), under the following locations:

L664246_D20180813T153001.413Z_stat_R000_tbb.h5

L703974_D20190424T213055.202Z_stat_R000_tbb.h5

all of them with the same prefix srm://srm.grid.sara.nl/pnfs/grid.sara.nl/data/lofar/ops/TBB/lightning/ and where “stat” should be replaced by the name of the station, CS001, CS002, CS003, CS004, CS005, CS006, CS007, CS011, CS013, CS017, CS021, CS024, CS026, CS030, CS031, CS032, CS101, CS103, RS106, CS201, RS205, RS208, RS210, CS301, CS302, RS305, RS306, RS307, RS310, CS401, RS406, RS407, RS409, CS501, RS503, or RS508. To access this data, please create an account following instructions at ASTRON (2020) and follow the instructions for “Staging Transient Buffer Board data.” In particular the utility “wget” should be used as in wget <https://lofar-download.grid.surfsara.nl/lofigrid/SRMFifoGet.py?url=location> where “location” is the location specified in the above.

Acknowledgments

The LOFAR cosmic ray key science project acknowledges funding from an Advanced Grant of the European Research Council (FP/2007-2013)/ERC Grant Agreement 227610. The project has also received funding from the European Research Council (ERC) under the European Union's Horizon 2020 research and innovation programme (Grant Agreement 640130). We further more acknowledge financial support from FOM (FOM-project 12PR304). B. M. Hare is supported by the NWO (VI.VENI.192.071). A. Nelles is supported by the DFG (NE 2031/2-1). T. Winchen is supported by DFG Grant 4946/1-1. The work of I. Kolmašová and O. Santolík was supported by the European Regional Development Fund-Project CREAT (CZ.02.1.01/0.0/0.0/15-003/0000481) and by the Praemium Academiae award of the Czech Academy of Sciences AS. The work of R. Lán and L. Uhlir was supported by the GACR Grant 20-09671S. K. Mulrey is supported by the FWO (FWO-12ZD920N). T. N. G. Trinh acknowledges funding from the Vietnam National Foundation for Science and Technology Development (NAFOSTED) under Grant 103.01-2019.378. S. Thoudam acknowledges funding from the Khalifa University Startup grant (project code 8474000237).

References

- ASTRON. (2020). *LOFAR long term archive access*. Retrieved from https://www.astron.nl/lofarwiki/doku.php?id=public:ita_howto
- Behnke, S. A., Thomas, R. J., Krehbiel, P. R., & Rison, W. (2005). Initial leader velocities during intracloud lightning: Possible evidence for a runaway breakdown effect. *Journal of Geophysical Research*, 110, D10207. <https://doi.org/10.1029/2004JD005312>
- Belz, J. W., Krehbiel, P. R., Remington, J., Stanley, M. A., Abbasi, R. U., LeVon, R., et al. (2020). Observations of the origin of downward terrestrial gamma-ray flashes. *Journal of Geophysical Research: Atmospheres*, 125, e2019JD031940. <https://doi.org/10.1029/2019JD031940>
- Bruning, E. C., Weiss, S. A., & Calhoun, K. M. (2014). Continuous variability in thunderstorm primary electrification and an evaluation of inverted-polarity terminology. *Atmospheric Research*, 135–136, 274–284. <https://doi.org/10.1016/j.atmosres.2012.10.009>
- Coleman, L. M., Stolzenburg, M., Marshall, T. C., & Stanley, M. (2008). Horizontal lightning propagation, preliminary breakdown, and electric potential in New Mexico thunderstorms. *Journal of Geophysical Research*, 113, D09208. <https://doi.org/10.1029/2007JD009459>
- Cummer, S. A., Lyu, F., Briggs, M. S., Fitzpatrick, G., Roberts, O. J., & Dwyer, J. R. (2015). Lightning leader altitude progression in terrestrial gamma-ray flashes. *Geophysical Research Letters*, 42, 7792–7798. <https://doi.org/10.1002/2015GL065228>
- Dennis, J., Gay, D., & Welsch, R. (1981). Algorithm 573: An adaptive nonlinear least-squares algorithm. *ACM Transactions on Mathematical Software*, 7(3), 367–383. <https://doi.org/10.1145/355958.355965>
- Dubnova, A., Rutjes, C., Ebert, U., Buitink, S., Scholten, O., & Trinh, G. T. N. (2015). Prediction of lightning inception by large ice particles and extensive air showers. *Physical Review Letters*, 115, 015002. <https://doi.org/10.1103/PhysRevLett.115.015002>
- Dwyer, J. R., & Uman, M. A. (2014). The physics of lightning. *Physics Reports*, 534(4), 147–241. <https://doi.org/10.1016/j.physrep.2013.09.004>
- Edens, H. E., Eack, K. B., Eastvedt, E. M., Trueblood, J. J., Winn, W. P., Krehbiel, P. R., & Thomas, R. J. (2012). VHF lightning mapping observations of a triggered lightning flash. *Geophysical Research Letters*, 39, L19807. <https://doi.org/10.1029/2012GL053666>
- Hare, B. M., Scholten, O., Bonardi, A., Buitink, S., Corstjan, A., Ebert, U., et al. (2018). LOFAR lightning imaging: Mapping lightning with nanosecond precision. *Journal of Geophysical Research: Atmospheres*, 123, 2861–2876. <https://doi.org/10.1002/2017JD028132>
- Hare, B. M., Scholten, O., Dwyer, J., Ebert, U., Nijdam, S., Bonardi, A., & Winchen, T. (2020). Radio emission reveals inner meter-scale structure of negative lightning leader steps. *Physical Review Letters*, 124, 105101. <https://doi.org/10.1103/PhysRevLett.124.105101>
- Hare, B. M., Scholten, O., Dwyer, J., Trinh, T. N. G., Buitink, S., ter Veen, S., et al. (2019). Needle-like structures discovered on positively charged lightning branches. *Nature*, 568, 360–363. <https://doi.org/10.1038/s41586-019-1086-6>
- Hill, J. D., Uman, M. A., & Jordan, D. M. (2011). High-speed video observations of a lightning stepped leader. *Journal of Geophysical Research*, 116, D16117. <https://doi.org/10.1029/2011JD015818>
- Kolmašová, I., Marshall, T., Bandara, S., Karunarathne, S., Stolzenburg, M., Karunarathne, N., & Siedlecki, R. (2019). Initial breakdown pulses accompanied by VHF pulses during negative cloud-to-ground lightning flashes. *Geophysical Research Letters*, 46, 5592–5600. <https://doi.org/10.1029/2019GL082488>
- Kolmašová, I., Santolík, O., Defer, E., Rison, W., Coquillat, S., Pedebay, S., & Pont, V. (2018). Lightning initiation: Strong pulses of VHF radiation accompany preliminary breakdown. *Scientific Reports*, 8(3650), 2045–2322. <https://doi.org/10.1038/s41598-018-21972-z>
- Kolmašová, I., Santolík, O., Farges, T., Rison, W., Lan, R., & Uhlir, L. (2014). Properties of the unusually short pulse sequences occurring prior to the first strokes of negative cloud-to-ground lightning flashes. *Geophysical Research Letters*, 41, 5316–5324. <https://doi.org/10.1002/2014GL060913>
- Kostinskiy, A. Y., Marshall, T. C., & Stolzenburg, M. (2019). The mechanism of the origin and development of lightning from initiating event to initial breakdown pulses. *Journal of Geophysical Research: Atmospheres*, 125(22), e2020JD033191. <https://doi.org/10.1029/2020JD033191>
- Krehbiel, P. (2017). Studies of lightning initiation. In *2017 XXXIIInd general assembly and scientific symposium of the international union of radio science* (pp. 1–2). URSI GASS. <https://doi.org/10.23919/URSIGASS.2017.8105171> lightningmaps.org. (n.d.). <http://Lightning-Maps.org>
- Lyu, F., Cummer, S. A., Lu, G., Zhou, X., & Weinert, J. (2016). Imaging lightning intracloud initial stepped leaders by low-frequency interferometric lightning mapping array. *Geophysical Research Letters*, 43, 5516–5523. <https://doi.org/10.1002/2016GL069267>
- Lyu, F., Cummer, S. A., Qin, Z., & Chen, M. (2019). Lightning initiation processes imaged with very high frequency broadband interferometry. *Journal of Geophysical Research: Atmospheres*, 124, 2994–3004. <https://doi.org/10.1029/2018JD029817>
- Mareev, E. A., & Dementyeva, S. O. (2017). The role of turbulence in thunderstorm, snowstorm, and dust storm electrification. *Journal of Geophysical Research: Atmospheres*, 122, 6976–6988. <https://doi.org/10.1002/2016JD026150>
- Marshall, T., Bandara, S., Karunarathne, N., Karunarathne, S., Kolmasova, I., Siedlecki, R., & Stolzenburg, M. (2019). A study of lightning flash initiation prior to the first initial breakdown pulse. *Atmospheric Research*, 217, 10–23. <https://doi.org/10.1016/j.atmosres.2018.10.013>

- Montanyà, J., van der Velde, O., & Williams, E. R. (2015). The start of lightning: Evidence of bidirectional lightning initiation. *Scientific Reports*, 5(1), 15180. <https://doi.org/10.1038/srep15180>
- Mulrey, K., Bonardi, A., Buitink, S., Corstanje, A., Falcke, H., Hare, B., & Winchen, T. (2019). Calibration of the LOFAR low-band antennas using the galaxy and a model of the signal chain. *Astroparticle Physics*, 111, 1–11. <https://doi.org/10.1016/j.astropartphys.2019.03.004>
- Pel, A. (2019). Imaging lightning with the extended Kalman filter (*master thesis*). University of Groningen, Faculty of Science and Engineering, KVI-CART. Retrieved from <http://fse.studenttheses.ub.rug.nl/id/eprint/19751>
- Proctor, D. E. (1991). Regions where lightning flashes began. *Journal of Geophysical Research*, 96(D3), 5099–5112. <https://doi.org/10.1029/90JD02120>
- Pu, Y., Cummer, S. A., & Retrieved from (2019). Needles and lightning leader dynamics imaged with 100–200 MHz broadband VHF interferometry. *Geophysical Research Letters*, 46, 13556–13563. <https://doi.org/10.1029/2019GL085635>
- Qi, Q., Lu, W., Ma, Y., Chen, L., Zhang, Y., & Rakov, V. A. (2016). High-speed video observations of the fine structure of a natural negative stepped leader at close distance. *Atmospheric Research*, 178–179, 260–267. <https://doi.org/10.1016/j.atmosres.2016.03.027>
- Rhodes, C. T., Shao, X. M., Krehbiel, P. R., Thomas, R. J., & Hayenga, C. O. (1994). Observations of lightning phenomena using radio interferometry. *Journal of Geophysical Research*, 99(D6), 13059–13082. <https://doi.org/10.1029/94JD00318>
- Rison, W., Krehbiel, P. R., Stock, M. G., Edens, H. E., Shao, X.-M., Thomas, R. J., & Zhang, Y. (2016). Observations of narrow bipolar events reveal how lightning is initiated in thunderstorms. *Nature Communications*, 7(1), 10721. <https://doi.org/10.1038/ncomms10721>
- Rison, W., Thomas, R. J., Krehbiel, P. R., Hamlin, T., & Harlin, J. (1999). A GPS-based three-dimensional lightning mapping system: Initial observations in central New Mexico. *Geophysical Research Letters*, 26(23), 3573–3576. <https://doi.org/10.1029/1999GL010856>
- Rutjes, C., Ebert, U., Buitink, S., Scholten, O., & Trinh, T. N. (2019). Generation of seed electrons by extensive air showers, and the lightning inception problem including narrow bipolar events. *Journal of Geophysical Research: Atmospheres*, 124, 7255–7269. <https://doi.org/10.1029/2018JD029040>
- Scholten, O. (2020). *A practical guide to lightning imaging with LOFAR (internal report)*. NL: Kapteyn Institute, University of Groningen. Retrieved from <https://www.astro.rug.nl/~scholten/Lightning/LOFLI.htm>
- Shao, X. M., & Krehbiel, P. R. (1996). The spatial and temporal development of intracloud lightning. *Journal of Geophysical Research*, 101(D21), 26641–26668. <https://doi.org/10.1029/96JD01803>
- Smith, E. M., Marshall, T. C., Karunarathne, S., Siedlecki, R., & Stolzenburg, M. (2018). Initial breakdown pulse parameters in intracloud and cloud-to-ground lightning flashes. *Journal of Geophysical Research: Atmospheres*, 123, 2129–2140. <https://doi.org/10.1002/2017JD027729>
- Stock, M. G., Akita, M., Krehbiel, P. R., Rison, W., Edens, H. E., Kawasaki, Z., & Stanley, M. A. (2014). Continuous broadband digital interferometry of lightning using a generalized cross-correlation algorithm. *Journal of Geophysical Research: Atmospheres*, 119, 3134–3165. <https://doi.org/10.1002/2013JD020217>
- Stolzenburg, M., Marshall, T. C., & Karunarathne, S. (2020). On the transition from initial leader to stepped leader in negative cloud-to-ground lightning. *Journal of Geophysical Research: Atmospheres*, 125, e2019JD031765. <https://doi.org/10.1029/2019JD031765>
- Tilles, J. N., Liu, N., Stanley, M. A., Krehbiel, P. R., Rison, W., Stock, M. G., & Wilson, J. (2019). Fast negative breakdown in thunderstorms. *Nature Communications*, 10(1), 1648. <https://doi.org/10.1038/s41467-019-09621-z>
- Tran, M. D., & Rakov, V. A. (2016). Initiation and propagation of cloud-to-ground lightning observed with a high-speed video camera. *Scientific Reports*, 6(1), 39521. <https://doi.org/10.1038/srep39521>
- Trinh, T. N. G., Scholten, O., Buitink, S., Ebert, U., Hare, B. M., Krehbiel, P. R., & Winchen, T. (2020). Determining electric fields in thunderclouds with the radiotelescope LOFAR. *Journal of Geophysical Research: Atmospheres*, 125, e2019JD031433. <https://doi.org/10.1029/2019JD031433>
- van Haarlem, M. P., Wise, M. W., Gunst, A. W., Heald, G., McKean, J. P., Hessels, J. W. T., et al. (2013). LOFAR: The LOW-Frequency ARray. *Astronomy and Astrophysics*, 556(A2), 53. <https://doi.org/10.1051/0004-6361/201220873>
- Yoshida, S., Biagi, C. J., Rakov, V. A., Hill, J. D., Stapleton, M. V., Jordan, D. M., & Kawasaki, Z.-I. (2010). Three-dimensional imaging of upward positive leaders in triggered lightning using VHF broadband digital interferometers. *Geophysical Research Letters*, 37, L05805. <https://doi.org/10.1029/2009GL042065>